Published in final edited form as:

ACS Appl Mater Interfaces. 2017 March 01; 9(8): 6772–6781. doi:10.1021/acsami.6b14049.

Intrinsic and Stable Conjugation of Thiolated Mesoporous Silica Nanoparticles with Radioarsenic

Paul A. Ellison[†,*], **Feng Chen**[‡], **Shreya Goel**[§], **Todd E. Barnhart**[†], **Robert J. Nickles**[†], **Onofre T. DeJesus**[†], and **Weibo Cai**[†,‡,§,||]

[†]Department of Medical Physics, University of Wisconsin School of Medicine and Public Health, Madison, Wisconsin 53726, United States

[‡]Department of Radiology, University of Wisconsin School of Medicine and Public Health, Madison, Wisconsin 53726, United States

[§]Materials Science Program, University of Wisconsin—Madison, Madison, Wisconsin 53706, United States

[||]Carbone Cancer Center, University of Wisconsin—Madison, Madison, Wisconsin 53706, United States

Abstract

The development of new image-guided drug delivery tools to improve the therapeutic efficacy of chemotherapeutics remains an important goal in nanomedicine. Using labeling strategies that involve radioelements that have theranostic pairs of diagnostic positron-emitting isotopes and therapeutic electron-emitting isotopes has promise in achieving this goal and further enhancing drug performance through radiotherapeutic effects. The isotopes of radioarsenic offer such theranostic potential and would allow for the use of positron emission tomography (PET) for image-guided drug delivery studies of the arsenic-based chemotherapeutic arsenic trioxide (ATO). Thiolated mesoporous silica nanoparticles (MSN) are shown to effectively and stably bind cyclotron-produced radioarsenic. Labeling studies elucidate that this affinity is a result of specific binding between trivalent arsenic and nanoparticle thiol surface modification. Serial PET imaging of the *in vivo* murine biodistribution of radiolabeled silica nanoparticles shows very good stability toward dearsenylation that is directly proportional to silica porosity. Thiolated MSNs are found to have a macroscopic arsenic loading capacity of 20 mg of ATO per gram of MSN, sufficient for delivery of chemotherapeutic quantities of the drug. These results show the great potential of

---

[*] Corresponding Author: paellison@wisc.edu (P.A.E.).

Present Address

F.C.: Memorial Sloan Kettering Cancer Center, New York, NY.

ORCID

Paul A. Ellison: 0000-0002-8379-7419

Author Contributions

P.A.E. and F.C. contributed equally to this work.

Notes

The authors declare no competing financial interest.

Supporting Information

The Supporting Information is available free of charge on the ACS Publications website at DOI: 10.1021/acsami.6b14049.

Equation S1: thiol groups per nanoparticle; Table S1: radioarsenic decay properties; Table S2: PET ROI results; Table S3: *ex vivo* biodistribution results; Figures S1–S3: additional *As-MSN labeling results (PDF)

radioarsenic-labeled thiolated MSN for the preparation of theranostic radiopharmaceuticals and image-guided drug delivery of ATO-based chemotherapeutics.

Graphical Abstract

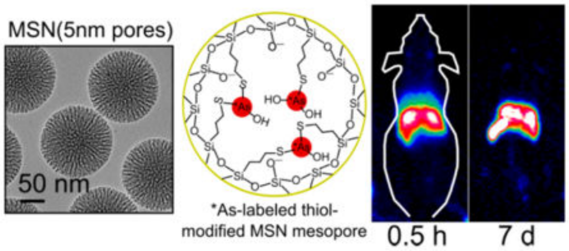

Keywords

image-guided drug delivery; arsenic trioxide; radioarsenic; positron emission tomography; As-72; As-76; As-77; radiolabeling

INTRODUCTION

Materials with particle size on the order of several to hundreds of nanometers are finding increasing application in medicine and biomedical research.[1,2] Notably among these is the development of nanomedicine-based drug delivery strategies for cancer therapy, where cytotoxic payloads are bound to nanoparticles, improving drug pharmacokinetics, targeting disease, and reducing systemic toxicity.[3,4] However, a recent survey of nanoparticle-based drug delivery platforms targeting solid tumors showed a very low median percentage of administered drug dose effectively being delivered to the tumor, highlighting a real need for image-guided drug delivery strategies to improve targeting efficacy.[5] Positron emission tomography (PET) is a noninvasive, quantitative imaging modality that requires radiolabeling with a positron-emitting nuclide, most commonly ^{64}Cu, ^{89}Zr, or ^{68}Ga when used in nanomedicine.[6] Because it is the biodistribution of this radionuclide, not the vehicle or payload, that is directly reported in a PET image, its use to provide image-guided drug delivery information is dependent on the efficacy of this radiolabeling strategy and the *in vivo* stability of the resulting conjugate. Anchoring the radiolabel to the nanoparticle is accomplished through one of several strategies, including functionalization of the vehicle with a chelator that has high affinity for the radiolabel[7–14] or through careful chemical pairing of the nanoparticle to a radionuclide with inherent affinity.[15–18] To fully take advantage of PET as an image-guided drug delivery tool, the *in vivo* stability of the radionuclide–nanoparticle conjugate for a new nanoparticle radiolabeling strategy must be carefully vetted.

The use of radiolabeling techniques to imbue nanoparticles with PET imaging capabilities has additional potential with the use of radionuclide-based theranostics, where the vehicle can be labeled alternatively with a chemically identical alpha-, Auger-, or electron-emitting radiotherapeutic nuclide. This pair of agents would then allow for the use of the diagnostic drug formulation to determine optimal therapeutic dose and gauge therapeutic response for the radiotherapeutic drug formulation, thereby facilitating suitable patient selection and minimizing adverse effects.[19,20] The radioisotopes of arsenic are well suited for use in theranostic pharmaceuticals in that there exist multiple positron-emitting diagnostic isotopes (^{71}As, ^{72}As, ^{74}As) and electron-emitting therapeutic isotopes (^{76}As, ^{77}As) with biologically relevant half-lives, as shown in Table S1. These radioisotopes can be produced in clinically relevant quantities through a variety of existing methods. Diagnostic ^{72}As can be produced using existing medical cyclotrons with solid target capability[21] or through a ^{72}Se/^{72}As generator system.[22,23] Therapeutic ^{77}As can be produced in a large-scale, yet still no-carrier-added, process using nuclear fission reactors.[24]

In addition to the potential of radioarsenic as a theranostic radiolabel, arsenic trioxide (ATO) is a United States Food and Drug Administration (FDA) approved drug (trade name: Trisenox at 0.15 mg/kg daily) that is current standard of care in combination with *all-trans*-retinoic acid for newly diagnosed and relapsed acute promyelocytic leukemia.[25] ATO has also been shown to be therapeutically effective at *in vitro* and preclinical *in vivo* studies toward other types of leukemia, lymphoid malignancies, and liver, gastric, ovarian, cervical, prostate, renal cell, bladder, brain, lung, and skin solid tumors.[26] However, the application of ATO is limited by its acute systemic toxicity estimated at ~0.6 mg/kg daily,[27] making ATO well suited for use as payload in nanoparticle-based drug delivery vehicles. Recent efforts to increase the therapeutic index of ATO have utilized a variety of nanoparticle-based drug delivery methods including liposomes,[28–31] polymeric nanoparticles, [32–35] and most recently mesoporous silica nanoparticles. [36–39]

Mesoporous silica nanoparticles (MSN) are a class of inorganic nanomaterial heavily permeated with open mesoporous channels with diameters on the order of 0.1–10 nm. The small particle size, porous nature, and silica framework result in a biocompatible material with extremely high specific surface area that has well-characterized surface chemistry allowing for its stable modification to exhibit a variety of chemically labile functional groups.[40] Thus, MSN is well suited for use as an image-guided drug delivery vehicle.[41] Previously, MSN has been radiolabeled with ^{64}Cu through surface-functionalized chelator-based methods[11,42] and through a chelator-free incorporation of ^{89}Zr and other radiometals in the silica framework.[18,43,44] Additionally, thiol-modified MSN has recently been shown to radiolabel with radioarsenic.[21] The present work aims to build upon this latter work and further characterize the arsenic–silica bioconjugation and *in vitro* and *in vivo* of thiolated-mesoporous-silica-bound radioarsenic.

RESULTS AND DISCUSSION

Synthesis and Characterization of Dense and Mesoporous Silica Nanoparticles

Three types of silica nanoparticles were synthesized and surface functionalized with sulfhydryl groups (–SH) to probe the radiolabeling and *in vivo* stability properties of the radioarsenic nanoparticle conjugates. The three types of silica differed by their nanoparticle diameter and porosity. They are dense silica (dSiO$_2$) nanoparticles (diameter of 90 ± 10 nm, no mesoporous channels) and two types of mesoporous silica nanoparticles (MSN): MSN (3 nm pores) (diameter of 65 ± 5 nm, ~3 nm diameter pores) and MSN (5 nm pores) (diameter of 150 ± 5 nm, ~5 nm diameter pores), as shown in Figure 1. The addition of thiol functional groups was accomplished in a surface area dependent manner through reaction with (3-mercaptopropyl)trimethoxysilane. The Brunauer–Emmett–Teller (BET) surface area and pore volume of the functionalized nanoparticles were measured and the latter used along with Ellman's reagent quantified thiol concentration and lyophilization measured mass concentration to calculate the number of thiol groups per nanoparticle for each of type of silica nanoparticle according to eq S1, shown in Table 1. Following synthesis, the thiol-modified silica nanoparticles were stored in solution with 5 mM tris(2-carboxyethyl) phosphine (TCEP) at pH 9 to prevent reduction of thiol concentration due to disulfide bond formation. Care was taken to remove TCEP through two subsequent 14 krpm centrifugation–decantation steps before quantifying nanoparticle thiol content using an Ellman's-reagent-based colorimetric method.

Production and Isolation of [*As]As(OH)$_3$

No-carrieradded (nca) [*As]arsenic trihydroxide (* = 72, 76, 74, 71) was produced through proton irradiation of metallic germanium and radiochemically isolated in a small volume, buffered aqueous solution. Overall decay-corrected radiochemical yield of the 4 h isolation procedure was 50 ± 1%. The use of natural isotopic abundance germanium target material produced radioarsenic with an end-of-bombardment isotopic composition of 79% ^{72}As, 0.2% ^{71}As, 14% ^{76}As, and 7% ^{74}As. The radioactive decay properties of ^{72}As ($t_{1/2}$ = 26.0 h, 88% β^+) and ^{74}As ($t_{1/2}$ = 17.8 d, 29% β^+) allowed for positron emission tomography (PET) imaging of radioarsenic for days (or weeks) after its production. The stability of the *As(III) oxidation state was monitored using autoradiography-visualized thin layer chromatography (radio-TLC) as a function of time in 0.1 M 4-(2-hydroxyethyl)-1-piperazineethanesulfonic acid (HEPES) with 70 mM hydroxylamine (HA) and 3 mM ethylenediamine-tetraacetic acid (EDTA) at two temperatures (21 and 80 °C) and three pHs (5.5, 7.5, and 9), shown in Figure 2. These results show that under nca conditions *As(III) is particularly susceptible to auto-oxidation, with the reaction promoted under high temperature and nonacidic conditions, despite the presence of HA and EDTA, which were found to improve As(III) stability. This auto-oxidation behavior of radioarsenic is of particular importance to this work as the reactivity of arsenic toward thiol groups is significantly greater for *As(III) compared with *As(V). To minimize the effects of auto-oxidation of *As(OH)$_3$ (As(III)) to *AsO(OH)$_3$ (As(V)) on the radiolabeling of thiol-modified nanoparticles, the final arsenic reduction and extraction procedure was performed immediately prior to the initiation of radiolabeling experiments.

Radioarsenic Labeling of MSN

The labeling yield of 590 nmol (–SH)/mL of thiol-modified MSN (3 nm pores) with nca *As(OH)$_3$ at pH 5.5, 7.5, and 9 as a function of time as determined by radio-TLC is shown partially in Figure 3a (blue line) and Figure S1b. These results clearly show *As-MSN labeling through the decrease of the *As(III) species concurrent with the increase of *As-MSN in the solution. The thiol specificity of the radioarsenic labeling was confirmed through a control experiment attempting to label amine-modified MSN with nca *As(OH)$_3$ at the same labeling conditions, shown in Figure 3a (red line) and Figure S1c. These results show no *As-MSN labeling with the arsenic speciation profile matching that of *As(OH)$_3$ in the aqueous labeling medium shown in Figure S1a. This infers that *As(III) is specifically binding to the soft base thiol functionality of the MSN-SH rather than nonspecifically binding to the silica framework or surface modification. The radioarsenic labeling of thiol-modified MSN was shown to be pH dependent with a higher labeling pH exhibiting significantly improved labeling yield, as shown in Figure 3c and Figure S1b. Higher labeling temperature (80 °C) was demonstrated to be unfavorable for labeling as shown in Figure 3b and Figure S2b. It was hypothesized that this was due to the rapid oxidation of *As(III) oxidation to *As(V) at higher temperature, shown Figure 2b. As shown in Figure S1b, the fraction of pentavalent arsenic species remains largely unchanged over the course of the labeling experiment, implying that *As(V) does not label thiol-modified MSN. This was further confirmed through an experiment attempting to label 480 nmol (–SH)/mL of MSN(3 nm pores)–SH with fully oxidized nca *$AsO(OH)_3$ at pH 9 (Figure 3d and Figure S3b) and 5.5 (Figure S3a) as a function of time. This clearly shows the negligible labeling yield of thiol-modified MSN with pentavalent radioarsenic. These results with nca radioarsenic are in good agreement with recent radioarsenic studies[45,46] and the well-established properties of bulk trivalent and pentavalent arsenic, as recently reviewed in the context of their protein binding properties,[47] which demonstrate high thiol binding for As(III) and negligible binding for As(V).

The concentration dependence of *As-MSN labeling was further examined by comparison of the labeling yield of 30, 60, 120, 240, 490, and 590 nmol (–SH)/mL MSN(3 nm pores)–SH with nca *$As(OH)_3$ at pH 9 as a function of time as shown in Figure 4. The radioarsenic labeling rate and yield after 24 h were found to be highly dependent on MSN (3 nm pores)–SH concentration, with higher concentrations correlating to higher labeling rates and 22 h labeling yields in the 70–80% range.

Labeling yields determined by radio-TLC were in good agreement with those obtained by radioactivity counting of the MSN pellet and supernatant following centrifugation and decantation. Radioarsenic labeling yields of thiol-modified $dSiO_2$ and MSN(5 nm pores) agreed well with the MSN(3 nm pores)-SH results. Optimal labeling yields of 80–90% were achieved under the most concentrated solutions achievable by directly reconstituting a centrifugation/decantation-isolated nanoparticle pellet in the *$As(OH)_3$ in 1 M HEPES, 0.5 M HA, 25 mM EDTA solution. Taken all together, we demonstrated the specific labeling of *As(III) to thiol-modified silica nanoparticles.

In Vitro and *in Vivo* Stability of Radioarsenic–MSN Bond

The *in vitro* stability of the binding of nca *$As(OH)_3$ to thiolated silica was probed by incubation of *As-MSN(3 nm pores) in whole mouse serum for 18 h at room temperature followed by 96 h at 37 °C with periodic monitoring of the radioarsenic speciation by radio-TLC with results shown in Figure 5. These results show a good stability of the *As–thiol–silica bond with greater than 80% of radioarsenic remaining bound to the nanoparticle over the 18 h of room temperature and first 2 days of 37 °C incubation.

The *in vivo* stability of radioarsenic binding to thiolated silica nanoparticles was monitored by comparison of the biodistribution of free *As with that of *As-MSN (3 nm pores) following intravenous (iv) injection in healthy mice as monitored by serial PET imaging. Characteristic maximum intensity projection (MIP) PET images are shown in Figures 6a and

6b, clearly demonstrating the marked difference in the biodistribution of these two radioarsenic preparations. Given the facts that highly negatively charged silica nanoparticles such as those used in this work are rapidly sequestered and retained for 7 days or longer by the liver and spleen,[18] that the nanoparticle size is larger than the renal clearance threshold of ~5 nm,[48] and the result that the majority of free radioarsenic is rapidly renally excreted (Figures 6a and 7a), the radiostability of the arsenic–thiol–silica bond can be monitored through the retention of radiotracer in the liver and the amount of radiotracer detected in the bladder. The PET-quantified percent injected dose per gram (%ID/g) measured for regions of interest (ROIs) surrounding the liver, spleen, and bladder for free *As and *As-MSN (3 nm pores) are shown in Table S2 and plotted in Figure 7b,c (red lines). The biodistribution of *As-MSN (3 nm pores) shows the rapid hepatic sequestration of the radioarsenic, persisting without significant change up to 3 days postinjection (Figure 7b, red line), in good agreement with those previously reported for ^{89}Zr–MSN.[18] At five and 7 days post injection, the PET signal in the liver appears to begin to drop, albeit not significantly (Figure 7b, red line) at all time points post injection. The quantified PET signal in the bladder was a consistent 4–5%ID/g (Figure 7c, red line). This result clearly demonstrates the good *in vivo* stability of the radioarsenic–thiolated MSN bond.

The *in vivo* stability of the *As–thiol–silica bond was further probed by comparing the biodistribution of *As-MSN(3 nm pores) with *As-dSiO$_2$ and *As-MSN(5 nm pores), which principally vary in their porosity, and therefore surface area and thiol density. Representative serial MIP PET images of *As-dSiO$_2$ and *As-MSN(5 nm pores) are shown in Figures 6c and 6d, respectively. ROI-based quantification of the %ID/g for these data are summarized in Table S2 and plotted in Figures 7b and 7c. The biodistribution of *As-dSiO$_2$ and *As-MSN(5 nm pores) at the time point immediately following injection are largely the same as *As-MSN(3 nm pores) with a large fraction (25–35%ID/g) of the dose immediately sequestered by the liver. However, one significant difference is that for *As-dSiO$_2$ a high activity fraction (>15%ID/g) was found in the bladder during the first two time points. While this high bladder uptake in *As-dSiO$_2$ is marked by a high interanimal standard deviation, it is indicative of a larger renal clearance rate of radioarsenic from the *As-dSiO$_2$ preparation. Because the size of the *As-dSiO$_2$ nanoparticles themselves are above the renal clearance size threshold, this uptake is attributable to desorbed free *As being rapidly renally excreted, as expected from the results in Figure 7a. Further evidence of the slow dearsenylation of *As-dSiO$_2$ is found in the steady and significant decrease in liver uptake (Figure 7b, blue line) over time since injection. In contrast to these results, *As-MSN(3 nm pores) and *As-MSN(5 nm pores) show very low (≤5%ID/g) uptake in the bladder for all time points and no observable decline in liver retention over at least 3 days postinjection. After 3 days postinjection, some decline in the *As-MSN(3 nm pores) liver uptake may be observed (Figure 7b, red line), while *As-MSN(5 nm pores) uptake increases (Figure 7b, yellow line). These results indicate a significant trend in stability toward dearsenylation, with the arsenic–thiol–silica bond stability progressing from the least stable *As-dSiO$_2$ to *As-MSN(3 nm pores) to *As-MSN(5 nm pores) as most stable. Several factors may be causing this trend in *in vivo* stability. One factor could be the larger mesoporosity fraction, as defined by the percent of overall nanoparticle volume that is the mesoporous channels, as calculated from BET pore volume and TEM radius and an assumed silica density of 2.2 g/mL to be 12% for

*As-dSiO$_2$, 51% for *As-MSN(3 nm pores), and 74% for *As-MSN(5 nm pores). It is possible that having a larger fraction of the nanoparticle surface area present inside the mesoporous channels would result in a higher fraction of the surfacebound *As within the mesoporous structure and therefore less accessible to dearsenylation as a result of trans-chelation with thiol-containing molecules and proteins *in vivo*. A second factor that may contribute to this trend in stability is the difference in surface thiol density, which is measured to be 71 thiol/nm^2 for *As-dSiO$_2$, 160 thiol/nm^2 for *As-MSN(3 nm pores), and 300 thiol/nm^2 for *As-MSN(5 nm pores). Thiol density likely plays a role in *in vivo* stability as a higher thiol density would result in a higher likelihood that a given surface *As would be bound by two or three thiols, thereby increasing its stability toward dearsenylation. *Ex vivo* biodistribution studies were performed following the final serial PET scan, with results shown in Figure 7d and Table S3. Comparison of the final scan's PET-quantified %ID/g with the *ex vivo* biodistribution resulted in good agreement, giving validity to the quantitative uptake values of the longitudinal, noninvasive PET imaging technique.

Arsenic Trioxide Loading Capacity of MSN

Recently, various forms of MSN have been investigated for use as drug delivery vehicles for the inorganic arsenic chemotherapeutic ATO,[37,38] including two utilizing thiolated MSN.[36,39] It is important to highlight that ATO, when dissolved in aqueous solution, takes an identical chemical form as the *As(OH)$_3$ produced in the radiochemical isolation procedure described above. To examine the overall capacity of the thiolated mesoporous silica used in this work for binding macroscopic quantities of ATO, 200 μg of MSN(5 nm pores) was incubated with 10^{-6}–10^{-3} g of $^{nat}As_2O_3$. The fraction of arsenic bound to MSN was then quantified using microwave-plasma atomic emission spectroscopy for the detection of elemental arsenic and silicon. The results of three arsenic loading capacity experiments are shown in Figure 8 plotting the concentration of silica-bound arsenic as milligrams of ATO per gram of MSN versus the concentration of nonbound arsenic as milligrams ATO per milliliter of labeling solution. This Langmuir-type plot is useful in determining the overall capacity of MSN for ATO loading, as when adsorption data are plotted linearly it appears as a rising curve reaching a plateau at the loading capacity. Thus, the ATO loading capacity for the MSN(5 nm pores) prepared in this work is ~20 mg/g. Comparison of this value with the number of thiols per gram of thiolated MSN(5 nm pores) (0.4 mmol of –SH/g) shows that this corresponds to a 1:2 molar ratio of As:thiols, implying that at full capacity two sulfhydryl groups are binding to each arsenic atom. This ATO loading capacity is also notably lower than that reported by Wu et al. of 120 mg/g[39] and Muhammad et al. of 46 mg/g[36] for other thiolated MSN preparations, likely as a result of a lower surface area (580 m^2/g vs 1021 m^2/g for Wu et al. and 728 m^2/g for Muhammad et al.) and thiol content (0.4 mmol of –SH/g vs 1.1 –SH/g for Wu et al.) of the MSN used in this work. Despite this, a loading capacity of 20 mg of ATO per gram of MSN is sufficient to deliver therapeutic quantities of 0.1–1 mg of ATO/kg with MSN doses of <50 mg of MSN/kg, which have been shown to be safe in murine models.[49] This shows the potential of [*As]ATO-MSN to combine chemotherapeutic properties of ATO with the diagnostic imaging properties of radioarsenic and the low toxicity, highly biocompatible drug delivery properties of MSN as a well tolerated image-guided drug delivery tool with high therapeutic index.

CONCLUSION

The radiolabeling of thiolated silica nanoparticles has been thoroughly investigated and shown to be a result of specific binding between *As(III) and thiol group surface modifications of the silica nanoparticles. Through the use of serial PET imaging, comparison of the *in vivo* murine biodistribution of three different *As-labeled thiolated silica nanoparticle morphologies was accomplished. It was concluded that the nanoparticles' *in vivo* stability toward dearsenylation is directly proportional to mesoporocity, likely as a result of the increased surface thiol density and higher fraction of internalized surface area. The *in vivo* stability observed for all thiolated silica nanoparticles was exceptionally good, with a large fraction of the radioarsenic remaining bound to the nanoparticle for days to weeks postinjection. This is a significant result as previous radioarsenic labeling strategies such as the direct labeling cysteine thiols of monoclonal antibodies have shown inadequately poor *in vivo* stability.[21] The high stability of radioarsenic binding to thiolated MSN, along with the facility of MSN toward additional modifications to improve blood retention and allow for passive and active targeting of solid tumors, makes this a very promising radiolabeling method for the production of radioarsenic-based theranostic pharmaceuticals. Additionally, the thiolated silica nanoparticles shown with the highest *in vivo* stability were investigated for macroscopic arsenic loading capacity using the chemotherapeutic ATO and shown to have a loading capacity of 20 mg of ATO per gram of nanoparticle. This shows the great potential of radioarsenic-labeled thiolated mesoporous silica for the development of a PET-guided ATO-based drug delivery strategy for improving the therapeutic efficacy of this versatile chemotherapeutic.

EXPERIMENTAL PROCEDURES

Materials

Unless otherwise stated, reagents were obtained from commercial vendors and used as received. Argon (industrial grade) and hydrogen gases (research grade, 99.9999% purity) were used.

Synthesis and Characterization of Dense and Mesoporous Silica Nanoparticles

Dense silica nanoparticles were synthesized using a modified Stöber method according to literature procedures.[18] Briefly, a solution of 35.7 mL of absolute ethanol, 5 mL of water, and 0.8 mL of ammonia was stirred at room temperature. Following the addition of 1 mL of tetraethyl orthosilicate (TEOS), the mixture was allowed to react for 1 h. The $dSiO_2$ were then washed through three cycles of 10 min, 14 krpm centrifugation followed by decantation and reconstitution in ethanol before resuspension in 20 mL of pure water.

Mesoporous silica nanoparticles with 2–3 nm mesopores were synthesized using a procedure adapted from the literature.[11] Briefly, 1 g of hexadecyltrimethylammonium chloride (CTAC) and 40 mg of triethylamine (TEA) were dissolved in 40 mL of water and stirred at room temperature for 1 h. Then, while stirring the mixture at 85 °C, 2 mL of TEOS was added at 0.33 mL/min, followed by 1 h of reaction at 90–95 °C. After the reaction, the MSN were collected by centrifugation at 12500*g* for 10 min, followed by decantation. The pellet was then reconstituted and stirred in 60 mL of 140 mM NaCl in methanol for 24 h, followed by pellet isolation through centrifugation and decantation. Repeating this NaCl/methanol washing process a total of three times has been shown to effectively removed the bulk of CTAC, as determined through the complete disappearance of the characteristic 2850 and 2921 cm^{-1} C–H peaks using Fourier transform infrared spectroscopy.[11]

Mesoporous silica nanoparticles with 5 nm pores were synthesized using a modified biphase stratification approach according to literature procedures.[18] Briefly, 24 mL of 25 wt % CTAC solution, 0.18 g of TEA, and 36 mL of water were stirred at 60 °C for 3 h. Then, following the careful addition of 20 mL of 20% v/v TEOS in cyclohexane, the solution was stirred at 125 rpm at 60 °C for 12 h. After the reaction, CTAC was removed from the MSN as described above.

Silica nanoparticles were surface modified to exhibit thiol or amine functional groups through reaction with (3-mercaptopropyl)-trimethoxysilane and (3-aminopropyl)trimethoxysilane, respectively, in absolute ethanol at 90 °C for 24–72 h.

Reaction with Ellman's reagent or 5,5′-dithiobis(2-nitrobenoic acid (DTNB) was used to quantify solution thiol concentration relative to freshly prepared 10–500 μM L-cysteine standards. 625 μL of reaction buffer (0.1 M Na_2HPO_4, 1 mM EDTA, pH 8), 13 μL of 10 mM DTNB, and 125 μL of standard or unknown were reacted for 15 min at room temperature, followed by absorbance measurement at 412 nm. A calibration curve based on the absorbance of L-cysteine standards was used.

Production and Isolation of [*As]As(OH)$_3$

No-carrier-added [*As]As$(OH)_3$ was produced using previously published methods.[21] Briefly, natural isotopic enrichment germanium metal was irradiated with 16 MeV protons using a GE PETtrace cyclotron. The irradiated metal was then dissolved in aqua regia while heating to 130 °C under a flow of argon. The solution was distilled to dryness, followed by the twice subsequent addition and distillation of 10 M HCl, 0.6% H_2O_2, effectively distilling the germanium target material as $GeCl_4$. The dried *As was then reconstituted in 10 M HCl and isolated from trace germanium and ^{67}Ga impurities through anion exchange (AX) chromatography. After AX purification, the *As, in its pentavalent As(V) oxidation state in ~10 mL of 10 M HCl, was reduced to trivalent *$AsCl_3$ through the addition of CuCl or KI and isolated in a small volume, neutral pH aqueous solution through liquid–liquid extraction (LLE) into cyclohexane or solid phase extraction (SPE) using a polystyrene–divinylbenzene (PS-DVB) resin (Chromabond HR-P). In the LLE procedure, the *$AsCl_3$ was twice extracted into an equal volume of cyclohexane, followed by the back-extraction of *As$(OH)_3$ into 500 μL of 0.1 M HEPES, 0.5 M HA, 25 mM EDTA at pH 7. In the SPE procedure, the *$AsCl_3$ was trapped on a 100 mg column of PS-DVB resin, followed by rinsing with 10 mL of 10 M HCl and eluted with 0.3–1 mL of 1 M HEPES, pH 9. After elution, NaOH, HA, and EDTA were added to bring the final formulation of *As$(OH)_3$ to contain 0.5 M HA, 25 mM EDTA at pH 7. The oxidation state of radioarsenic throughout and after the radiochemical procedure was assessed using autoradiography-visualized SiO_2 radio-TLC using 3:1::0.01 M sodium tartrate:methanol as mobile phase,[50] with *As(III) migrating to a retention factor (R_f) of 0.6–0.8 and *As(V) to a R_f of 0.9–1. Trace metal analysis was performed using microwave plasma atomic emission spectroscopy (MP-AES, MP-4200, Agilent Technologies) with limits of detection for arsenic, germanium, and copper in the final $^*As(OH)_3$ preparation of 10 ppm, 1 ppm, and 10 ppb, respectively.

Radioarsenic Labeling of MSN

Radioarsenic labeling of surface-modified silica nanoparticles was performed in room temperature, buffered aqueous solutions. First, $dSiO_2$, MSN(3 nm pores), or MSN(5 nm pores) (0.05–15 mg Si, 40–200 nmol of –SH or $–NH_2$) were isolated by centrifugation at 14 krpm for 10 min followed by decantation. The pellet was then reconstituted in 0.4–180 MBq of freshly LLE- or SPE-prepared $^*As(OH)_3$ in 0.1–1 M HEPES containing 70–500 mM HA, 3–25 mM EDTA at pH 5.5, 7.5, or 9. Progression of the radiolabeling was longitudinally assessed using the above-described radio-TLC procedure, with the As-MSN demonstrating a R_f of 0. At the end of the labeling study, the labeling efficacy was also determined by dose calibrator (CRC-15, Capintec, Inc.) measurement of the *As-MSN pellet and free *As(III)/ *As(V) in the supernatant following 10 min 14 000 rpm centrifugation and decantation.

In Vitro and *in Vivo* Stability of Radioarsenic–MSN Bond

The *in vitro* stability of the binding of radioarsenic to thiolated silica nanoparticles was assessed by incubation of *As-MSN(3 nm pores) in whole mouse serum for 18 h at room temperature, followed by 4 days at 37 °C. Radiolabeled *As-MSN(3 nm pores) were twice washed with water by repeated centrifugation and decantation and then reconstituted in whole mouse serum. This and a control vial containing free *As in whole mouse serum and 12 mM EDTA, 0.25 M HA, and 50 mM HEPES, pH 7.5 were incubated and monitored for silica-bound radioarsenic fraction using the above-described radio-TLC procedure.

The *in vivo* stability of the binding of radioarsenic to thiolated silica nanoparticles was assessed through serial PET imaging of mice following the injection of nca *As, $^*As\text{-}dSiO_2$, *As-MSN(3 nm pores), and *As-MSN(5 nm pores). For nanoparticle labeling, $dSiO_2$ (16 mg of Si, 75 nmol of thiol), MSN(3 nm pores) (2.8 mg of Si, 180 nmol of thiol), or MSN(5 nm pores) (2.1 mg of Si, 620 nmol of thiol) were isolated by 14k centrifugation and decantation and combined with 300–650 μL of freshly LLE- or SPE-prepared nca $^*As(OH)_3$ in 0.1–1 M HEPES, 0.12–0.5 M HA, 6–25 mM EDTA and incubated at room temperature overnight, giving a radiolabeling yield of 40–90%. The resulting radiolabeled nanoparticles were isolated by centrifugation and decantation, followed by washing twice with 500 μL of water through subsequent sonication-assisted reconstitution, recentrifugation, and decantation with the final pellet reconstituted in 0.4–1.5 mL of phosphate-buffered saline for injection. Free *As was prepared immediately before injection by dilution of LLE-prepared nca $^*As(OH)_3$ in phosphate buffered saline, giving a final concentration of 7 mM HEPES, 30 mM HA, and 2 mM EDTA.

Twelve healthy BALB/c mice (three per radioarsenic preparation) were tail-vein-injected each with nca *As (200 μL, 10 MBq), $^*As\text{-}dSiO_2$ (200 μL, 2.8–3.0 MBq, 3.2 mg of SiO_2), *As-MSN(3 nm pores) (95–170 μL, 2.5–4.4 MBq, 0.6–1.0 mg of SiO_2), or *As-MSN(5 nm pores) (120–200 μL, 5.9–10 MBq, 0.1–0.2 mg of SiO_2). Prior to injection, the radioactivity in each injected dose was measured in a dose calibrator (CRC-15, Capintec, Inc., Ramsey, NJ) with setting #970.[21] Additionally, a 10 μL aliquot from each injected dose was measured using efficiency-calibrated high purity germanium (HPGe) gamma spectroscopy (Canberra Industries, Inc., Meridian, CT) to determine the radioarsenic isotopic distribution. While this radio-isotopic purity is found to be >99% ^{72}As for radioarsenic produced using isotopically enriched ^{72}Ge target material,[21] when natural-enrichment germanium target material was utilized, it was found to be a mixture of positron-emitting isotopes at the time of injection with ~80% ^{72}As (26.0 h, 88% β+), ~10% ^{74}As (17.8 d, 29% β+), 2–3% ^{71}As (65.3 h, 27.9% β+ emission), and ~9% the electron-emitting isotope ^{76}As (26.4 h). Following injection, serial PET images were obtained at various times from 0.5 to 189 h postinjection using an Inveon microPET scanner (Siemens Medical Solutions USA, Inc., Malvern, PA) at the University of Wisconsin Carbone Cancer Center Small Animal Imaging Facility. The images were reconstructed with an OSEM3D algorithm with neither attenuation nor scatter correction. For each PET scan, three-dimensional ROIs were drawn over the liver, spleen, and bladder using vendor software (Inveon Research Workshop). With an assumed tissue density of 1 g/mL, the raw PET data were converted to MBq/g using a conversion factor that was predetermined by PET quantification of a 50 mL cylinder containing a known quantity of *As solution. This value was then divided by the total injected decay- and positron-branching-ratio-corrected radioactivity as measured by dose calibrator and HPGe measurements to determine the PET-image derived %ID/g.

Ex vivo biodistribution studies were performed following each final serial PET scan. All major organs were collected, wet-weighed and assayed using a well-type gamma counter (PerkinElmer, Waltham, MA). One representative sample was also assayed by efficiency-calibrated HPGe gamma spectroscopy to determine the absolute efficiency calibration of the well-type gamma counter for the mixture of radioarsenic isotopes.

Arsenic Trioxide Loading Capacity of MSN

The loading capacity of MSN(5 nm pores) for macroscopic natural abundance arsenic was evaluated through a series of ATO binding assays. Thiol-modified MSN(5 nm pores) was thrice washed with water, reconstituted in 200–500 μL of 0.05–0.1 M HEPES buffer, pH 7–9 containing 3 μg–1 mg of ATO, and incubated at room temperature for 3–11 days. After incubation, ATO-MSN(5 nm pores) were isolated by centrifugation/decantation and washed once with 0.1 M HEPES. The ATO-MSN(5 nm pores) pellet was reconstituted in 0.1 M HEPES, and microwave plasma atomic emission spectroscopy was performed on the reconstituted pellet, the first supernatant (labeling solution), second supernatant (wash solution), and 10× dilutions of the reconstituted pellet and labeling solution, quantifying arsenic and silicon mass. The quantified masses of arsenic and silicon in each solution were used to calculate the concentration of silica-bound arsenic as milligrams of ATO per gram of MSN and the concentration of nonbound arsenic remaining in the labeling and wash solutions as milligrams of ATO per milliliter of labeling solution.

Supplementary Material

Refer to Web version on PubMed Central for supplementary material.

Acknowledgments

This work was supported in part by the University of Wisconsin—Madison, U.S. Department of Energy under Grants DE-SC0005281 and DE-SC0008384, National Institutes of Health under Grant T32CA009206 and 1R0-1CA169365, the American Cancer Society under Grant 125246-RSG-13-099-01-CCE, and the University of Wisconsin Carbone Cancer Center Support Grant P30 CA014520.

References

1. De M, Ghosh PS, Rotello VM. Applications of Nanoparticles in Biology. Adv Mater. 2008; 20:4225–4241.
2. Jain RK, Stylianopoulos T. Delivering Nanomedicine to Solid Tumors. Nat Rev Clin Oncol. 2010; 7:653–664. [PubMed: 20838415]
3. Peer D, Karp JM, Hong S, Farokhzad OC, Margalit R, Langer R. Nanocarriers as an Emerging Platform for Cancer Therapy. Nat Nanotechnol. 2007; 2:751–760. [PubMed: 18654426]
4. Chow EKH, Ho D. Cancer Nanomedicine: From Drug Delivery to Imaging. Sci Transl Med. 2013; 5:216rv4.
5. Wilhelm S, Tavares AJ, Dai Q, Ohta S, Audet J, Dvorak HF, Chan WCW. Analysis of Nanoparticle Delivery to Tumors. Nat Rev Mater. 2016; 1:16014.
6. Sun X, Cai W, Chen X. Positron Emission Tomography Imaging Using Radiolabeled Inorganic Nanomaterials. Acc Chem Res. 2015; 48:286–294. [PubMed: 25635467]
7. Sun X, Rossin R, Turner JL, Becker ML, Joralemon MJ, Welch MJ, Wooley KL. An Assessment of the Effects of Shell Cross-Linked Nanoparticle Size, Core Composition, and Surface PEGylation on In Vivo Biodistribution. Biomacromolecules. 2005; 6:2541–2554. [PubMed: 16153091]
8. Jarrett BR, Gustafsson B, Kukis DL, Louie AY. Synthesis of 64Cu-Labeled Magnetic Nanoparticles for Multimodal Imaging. Bioconjugate Chem. 2008; 19:1496–1504.
9. Wang Y, Liu Y, Luehmann H, Xia X, Brown P, Jarreau C, Welch M, Xia Y. Evaluating the Pharmacokinetics and *In Vivo* Cancer Targeting Capability of Au Nanocages by Positron Emission Tomography Imaging. ACS Nano. 2012; 6:5880–5888. [PubMed: 22690722]
10. Hong H, Yang K, Zhang Y, Engle JW, Feng L, Yang Y, Nayak TR, Goel S, Bean J, Theuer CP, Barnhart TE, Liu Z, Cai W. In Vivo Targeting and Imaging of Tumor Vasculature with Radiolabeled, Antibody-Conjugated Nanographene. ACS Nano. 2012; 6:2361–2370. [PubMed: 22339280]
11. Chen F, Hong H, Zhang Y, Valdovinos HF, Shi S, Kwon GS, Theuer CP, Barnhart TE, Cai W. In Vivo Tumor Targeting and Image-Guided Drug Delivery with Antibody-Conjugated, Radiolabeled Mesoporous Silica Nanoparticles. ACS Nano. 2013; 7:9027–9039. [PubMed: 24083623]
12. Keliher EJ, Yoo J, Nahrendorf M, Lewis JS, Marinelli B, Newton A, Pittet MJ, Weissleder R. ^{89}Zr-Labeled Dextran Nanoparticles Allow in Vivo Macrophage Imaging. Bioconjugate Chem. 2011; 22:2383–2389.
13. Majmudar MD, Yoo J, Keliher EJ, Truelove JJ, Iwamoto Y, Sena B, Dutta P, Borodovsky A, Fitzgerald K, Di Carli MF, Libby P, Anderson DG, Swirski FK, Weissleder R, Nahrendorf M. Polymeric Nanoparticle PET/MR Imaging Allows Macrophage Detection in Atherosclerotic Plaques. Circ Res. 2013; 112:755–761. [PubMed: 23300273]
14. Pérez-Medina C, Abdel-Atti D, Tang J, Zhao Y, Fayad ZA, Lewis JS, Mulder WJM, Reiner T. Nanoreporter PET Predicts the Efficacy of Anti-Cancer Nanotherapy. Nat Commun. 2016; 7:11838. [PubMed: 27319780]
15. Zhou M, Zhang R, Huang M, Lu W, Song S, Melancon MP, Tian M, Liang D, Li C. A Chelator-Free Multifunctional [^{64}Cu]CuS Nanoparticle Platform for Simultaneous Micro-PET/CT Imaging and Photothermal Ablation Therapy. J Am Chem Soc. 2010; 132:15351–15358. [PubMed: 20942456]
16. Chen F, Ellison PA, Lewis CM, Hong H, Zhang Y, Shi S, Hernandez R, Meyerand ME, Barnhart TE, Cai W. Chelator-Free Synthesis of a Dual-Modality PET/MRI Agent. Angew Chem, Int Ed. 2013; 52:13319–13323.

17. Boros E, Bowen AM, Josephson L, Vasdev N, Holland JP. Chelate-Free Metal Ion Binding and Heat-Induced Radiolabeling of Iron Oxide Nanoparticles. Chem Sci. 2015; 6:225–236. [PubMed: 28553472]

18. Chen F, Goel S, Valdovinos HF, Luo H, Hernandez R, Barnhart TE, Cai W. In Vivo Integrity and Biological Fate of Chelator-Free Zirconium-89-Labeled Mesoporous Silica Nanoparticles. ACS Nano. 2015; 9:7950–7959. [PubMed: 26213260]

19. Lammers T, Aime S, Hennink WE, Storm G, Kiessling F. Theranostic Nanomedicine. Acc Chem Res. 2011; 44:1029–1038. [PubMed: 21545096]

20. Kelkar SS, Reineke TM. Theranostics: Combining Imaging and Therapy. Bioconjugate Chem. 2011; 22:1879–1903.

21. Ellison PA, Barnhart TE, Chen F, Hong H, Zhang Y, Theuer CP, Cai W, Nickles RJ, DeJesus OT. High Yield Production and Radiochemical Isolation of Isotopically Pure Arsenic-72 and Novel Radioarsenic Labeling Strategies for the Development of Theranostic Radiopharmaceuticals. Bioconjugate Chem. 2016; 27:179–188.

22. Ballard B, Wycoff D, Birnbaum ER, John KD, Lenz JW, Jurisson SS, Cutler CS, Nortier FM, Taylor WA, Fassbender ME. Selenium-72 Formation Via ^{nat}Br(p,x) Induced by 100 MeV Protons: Steps Toward a Novel ^{72}Se/^{72}As Generator System. Appl Radiat Isot. 2012; 70:595–601. [PubMed: 22326368]

23. Chajduk E, Doner K, Polkowska-Motrenko H, Bilewicz A. Novel Radiochemical Separation of Arsenic from Selenium for ^{72}Se/^{72}As Generator. Appl Radiat Isot. 2012; 70:819–822. [PubMed: 22342310]

24. Bokhari TH, Mushtaq A, Khan IU. Separation of No-Carrier-Added Arsenic-77 from Neutron Irradiated Germanium. Radiochim Acta. 2009; 97:503–506.

25. Lo-Coco F, Avvisati G, Vignetti M, Thiede C, Orlando SM, Iacobelli S, Ferrara F, Fazi P, Cicconi L, Di Bona E, Specchia G, Sica S, Divona M, Levis A, Fiedler W, Cerqui E, Breccia M, Fioritoni G, Salih HR, Cazzola M, Melillo L, Carella AM, Brandts CH, Morra E, von Lilienfeld-Toal M, Hertenstein B, Wattad M, Lübbert M, Hänel M, Schmitz N, Link H, Kropp MG, Rambaldi A, La Nasa G, Luppi M, Ciceri F, Finizio O, Venditti A, Fabbiano F, Döhner K, Sauer M, Ganser A, Amadori S, Mandelli F, Döhner H, Ehninger G, Schlenk RF, Platzbecker U. Retinoic Acid and Arsenic Trioxide for Acute Promyelocytic Leukemia. N Engl J Med. 2013; 369:111–121. [PubMed: 23841729]

26. Dilda PJ, Hogg PJ. Arsenical-Based Cancer Drugs. Cancer Treat Rev. 2007; 33:542–564. [PubMed: 17624680]

27. Ratnaike RN. Acute and Chronic Arsenic Toxicity. Postgrad Med J. 2003; 79:391–396. [PubMed: 12897217]

28. Ahn RW, Chen F, Chen H, Stern ST, Clogston JD, Patri AK, Raja MR, Swindell EP, Parimi V, Cryns VL, O’Halloran TV. A Novel Nanoparticulate Formulation of Arsenic Trioxide with Enhanced Therapeutic Efficiacy in a Murine Model of Breast Cancer. Clin Cancer Res. 2010; 16:3607–3617. [PubMed: 20519360]

29. Ahn RW, Barrett SL, Raja MR, Jozefik JK, Spaho L, Chen H, Bally MB, Mazar AP, Avram MJ, Winter JN, Gordon LI, Shea LD, O’Halloran TV, Woodruff TK. Nano-Encapsulation of Arsenic Trioxide Enhances Efficacy against Murine Lymphoma Model while Minimizing Its Impact on Ovarian Reserve *In Vitro* and *In Vivo*. PLoS One. 2013; 8:e58491. [PubMed: 23526987]

30. Zhang L, Zhang Z, Mason RP, Sarkaria JN, Zhao D. Convertible MRI Contrast: Sensing the Delivery and Release of Anti-Glioma Nano-Drugs. Sci Rep. 2015; 5:9874. [PubMed: 25962872]

31. Wang X, Li D, Ghali L, Xia R, Munoz LP, Garelick H, Bell C, Wen X. Therapeutic Potential of Delivering Arsenic Trioxide into HPV-Infected Cervical Cancer Cells Using Liposomal Nanotechnology. Nanoscale Res Lett. 2016; 11:94. [PubMed: 26887578]

32. Qian C, Wang Y, Chen Y, Zeng L, Zhang Q, Shuai X, Huang K. Suppression of Pancreatic Tumor Growth by Targeted Arsenic Delivery with Anti-CD44v6 Single Chain Antibody Conjugated Nanoparticles. Biomaterials. 2013; 34:6175–6184. [PubMed: 23721794]

33. Zeng L, Li J, Wang Y, Qian C, Chen Y, Zhang Q, Wu W, Lin Z, Liang J, Shuai X, Huang K. Combination of siRNA-Directed Kras Oncogene Silencing and Arsenic-Induced Apoptosis Using

a Nanomedicine Strategy for the Effective Treatment of Pancreatic Cancer. Nanomedicine. 2014; 10:463–472. [PubMed: 24028894]

34. Zhang Q, Vakili MR, Li XF, Lavasanifar A, Le XC. Polymeric Micelles for GSH-Triggered Delivery of Arsenic Species to Cancer Cells. Biomaterials. 2014; 35:7088–7100. [PubMed: 24840615]
35. Jadhav V, Ray P, Sachdeva G, Bhatt P. Biocompatible Arsenic Trioxide Nanoparticles Induce Cell Cycle Arrest by $p23^{WAF1/CIP1}$ Expression *Via* Epigenetic Remodeling in LNCaP and PC3 Cell Lines. Life Sci. 2016; 148:41–52. [PubMed: 26883975]
36. Muhammad F, Zhao J, Wang N, Guo M, Wang A, Chen L, Guo Y, Li Q, Zhu G. Lethal Drug Combination: Arsenic Loaded Multiple Drug Mesoporous Slica for Theranostic Applications. Colloids Surf, B. 2014; 123:506–514.
37. Zhao Z, Wang X, Zhang Z, Zhang H, Liu H, Zhu X, Li H, Chi X, Yin Z, Gao J. Real-Time Monitoring of Arsenic Trioxide Release and Delivery by Activatable T_1 Imaging. ACS Nano. 2015; 9:2749–2759. [PubMed: 25688714]
38. Zhao Z, Zhang H, Chi X, Li H, Yin Z, Huang D, Wang X, Gao J. Silica Nanovehicles Endow Arsenic Trioxide with an Ability to Effectively Treat Cancer Cells and Solid Tumors. J Mater Chem B. 2014; 2:6313–6323.
39. Wu X, Han Z, Schur RM, Lu ZR. Targeted Mesoporous Silica Nanoparticles Delivering Arsenic Trioxide with Environment Sensitive Drug Release for Effective Treatment of Triple Negative Breast Cancer. ACS Biomater Sci Eng. 2016; 2:501–507.
40. Tang F, Li L, Chen D. Mesoporous Silica Nanoparticles: Synthesis, Biocompatibility and Drug Delivery. Adv Mater. 2012; 24:1504–1534. [PubMed: 22378538]
41. Yang P, Gai S, Lin J. Functionalized Mesoporous Silica Materials for Controlled Drug Delivery. Chem Soc Rev. 2012; 41:3679–3698. [PubMed: 22441299]
42. Chen F, Hong H, Shi S, Goel S, Valdovinos HF, Hernandez R, Theuer CP, Barnhart TE, Cai W. Engineering of Hollow Mesoporous Silica Nanoparticles for Remarkably Enhanced Tumor Active Targeting Efficacy. Sci Rep. 2014; 4:5080. [PubMed: 24875656]
43. Shaffer TM, Wall MA, Harmsen S, Longo VA, Drain CM, Kircher MF, Grimm J. Silica Nanoparticles as Substrates for Chelator-free Labeling of Oxophilic Radioisotopes. Nano Lett. 2015; 15:864–868. [PubMed: 25559467]
44. Shaffer TM, Harmsen S, Khwaja E, Kircher MF, Drain CM, Grimm J. Stable Radiolabeling of Sulfur-Functionalized Silica Nanoparticles with Copper-64. Nano Lett. 2016; 16:5601–5604. [PubMed: 27464258]
45. DeGraffenreid AJ, Feng Y, Barnes CL, Ketring AR, Cutler CS, Jurisson SS. Trithiols and their arsenic compounds for potential use in diagnostic and therapeutic radiopharmaceuticals. Nucl Med Biol. 2016; 43:288–295. [PubMed: 27150031]
46. DeGraffenreid AJ, Feng Y, Wycoff DE, Morrow R, Phipps MD, Cutler CS, Ketring AR, Barnes CL, Jurisson SS. Dithiol Aryl Arsenic Compounds as Potential Diagnostic and Therapeutic Radiopharmaceuticals. Inorg Chem. 2016; 55:8091–8098. [PubMed: 27453472]
47. Chen B, Liu Q, Popowich A, Shen S, Yan X, Zhang Q, Li XF, Weinfeld M, Cullen WR, Le XC. Therapeutic and Analytical Applications of Arsenic Binding to Proteins. Metallomics. 2015; 7:39–55. [PubMed: 25356501]
48. Choi HK, Liu W, Misra P, Tanaka E, Zimmer JP, Itty Ipe BI, Bawendi MG, Frangioni JV. Renal Clearance of Nanoparticles. Nat Biotechnol. 2007; 25:1165–1170. [PubMed: 17891134]
49. Lu J, Liong M, Li Z, Zink JI, Tamanoi F. Biocompatability, Biodistribution, and Drug-Delivery Efficiency of Mesoporous Silica Nanoparticles for Cancer Therapy in Animals. Small. 2010; 6:1794–1805. [PubMed: 20623530]
50. Jahn M, Radchenko V, Filosofov D, Hauser H, Eisenhut M, Rösch F, Jennewein M. Separation and Purification of No-Carrier-Added Arsenic from Bulk Amounts of Germanium for Use in Radiopharmaceutical Labelling. Radiochim Acta. 2010; 98:807–812.

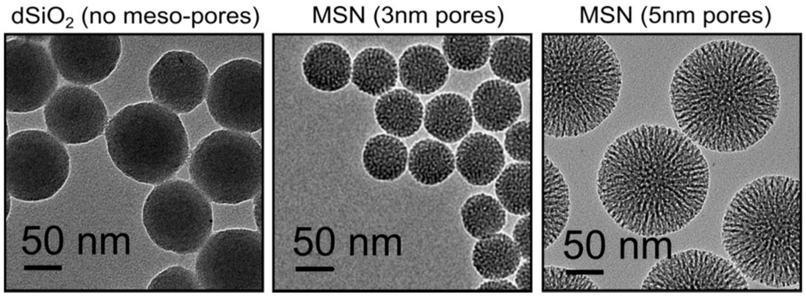

Figure 1.

Transmission electron microscopy images of three types of silica nanoparticles used for radioarsenic labeling and affinity studies.

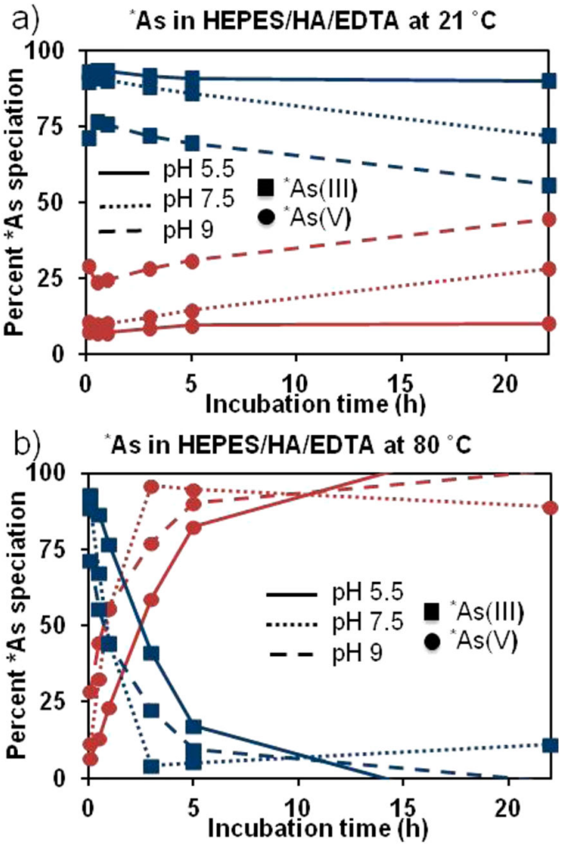

Figure 2.

Stability of *As(III) oxidation state toward auto-oxidation to *As(V) in 0.1 M HEPES, 0.5 M HA, 25 mM EDTA at various pH, temperatures. Plots show the changes of percent of *As(III) (blue squares) and *As(V) (red circles) in solutions at pH 5.5 (solid lines), pH 7.5 (dotted lines), and pH 9 (dashed lines) at (a) 21 °C and (b) 80 °C. While uncertainties were not quantified in these radio-TLC studies, the methods resulted in high uncertainty estimated to be ~15% in solutions containing nearly 0% *As(III) and nearly 100% *As(V).

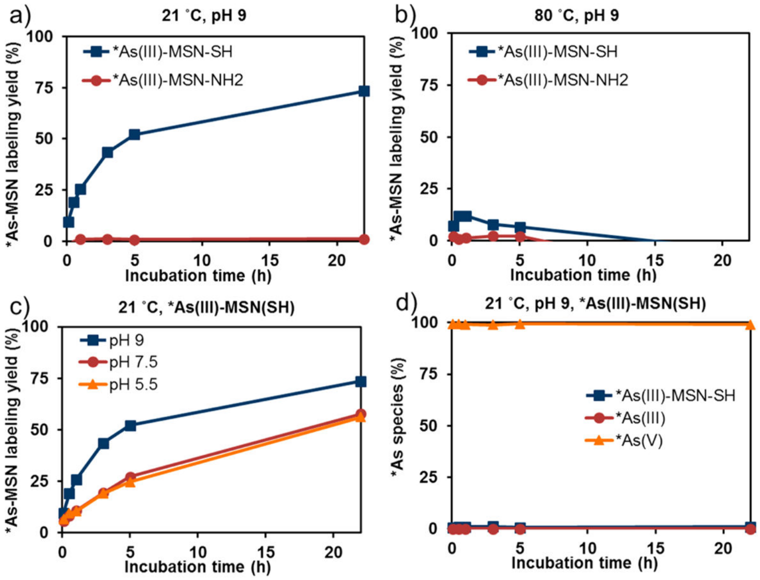

Figure 3.

Representative labeling results of MSN(3 nm pores)–SH (600 nmol [–SH]/mL) and MSN(3 nm pores)–NH_2 (520 nmol [–NH_2]/mL) with *As$(OH)_3$ in 0.1 M HEPES, 70 mM HA, 3 mM EDTA solutions. (a) Labeling temperature was set to be 21 °C. (b) Labeling temperature was set to be 80 °C. (c) Labeling results of MSN(3 nm pores)–SH (600 nmol [–SH]/mL) with *As$(OH)_3$ in 0.1 M HEPES, 70 mM HA, 3 mM EDTA solutions, under varied pH conditions, pH 5.5, 7.5, and 9, at 21 °C. (d) Labeling results of 490 nmol (–SH)/mL MSN(3 nm pores)–SH with *AsO$(OH)_3$ in 0.1 M HEPES, 0.14 M HA, 7 mM EDTA solutions at pH 7.5, 21 °C. While uncertainties were not quantified in these radio-TLC studies, the methods resulted in high uncertainty estimated to be ~15% in solutions containing nearly 0% *As(III) or *As-MSN or 100% *As(V).

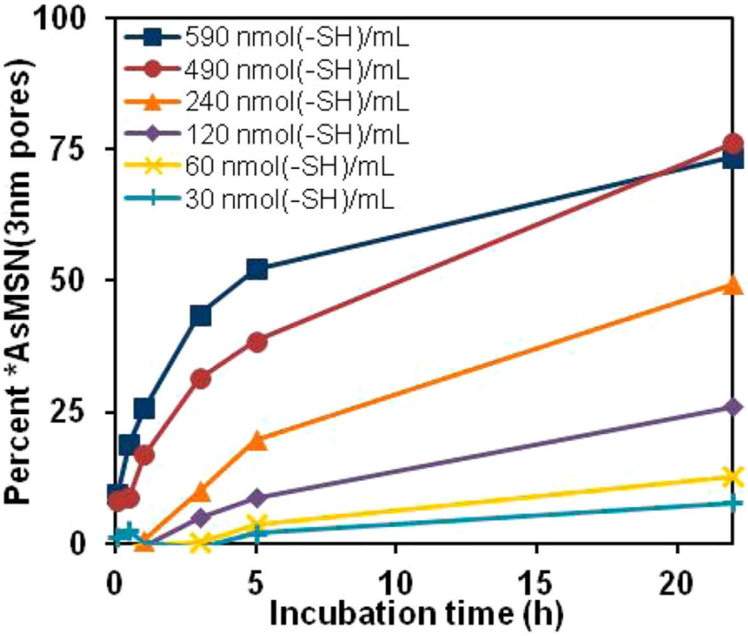

Figure 4.

Labeling results of various concentrations of MSN(3 nm pores)–SH with $^*As(OH)_3$ in 0.1 M HEPES, 70 mM HA, 3 mM EDTA solutions at pH 9. While uncertainties were not quantified in these radio-TLC studies, the methods resulted in high uncertainty estimated to be ~15% in solutions containing nearly 0% *As-MSN.

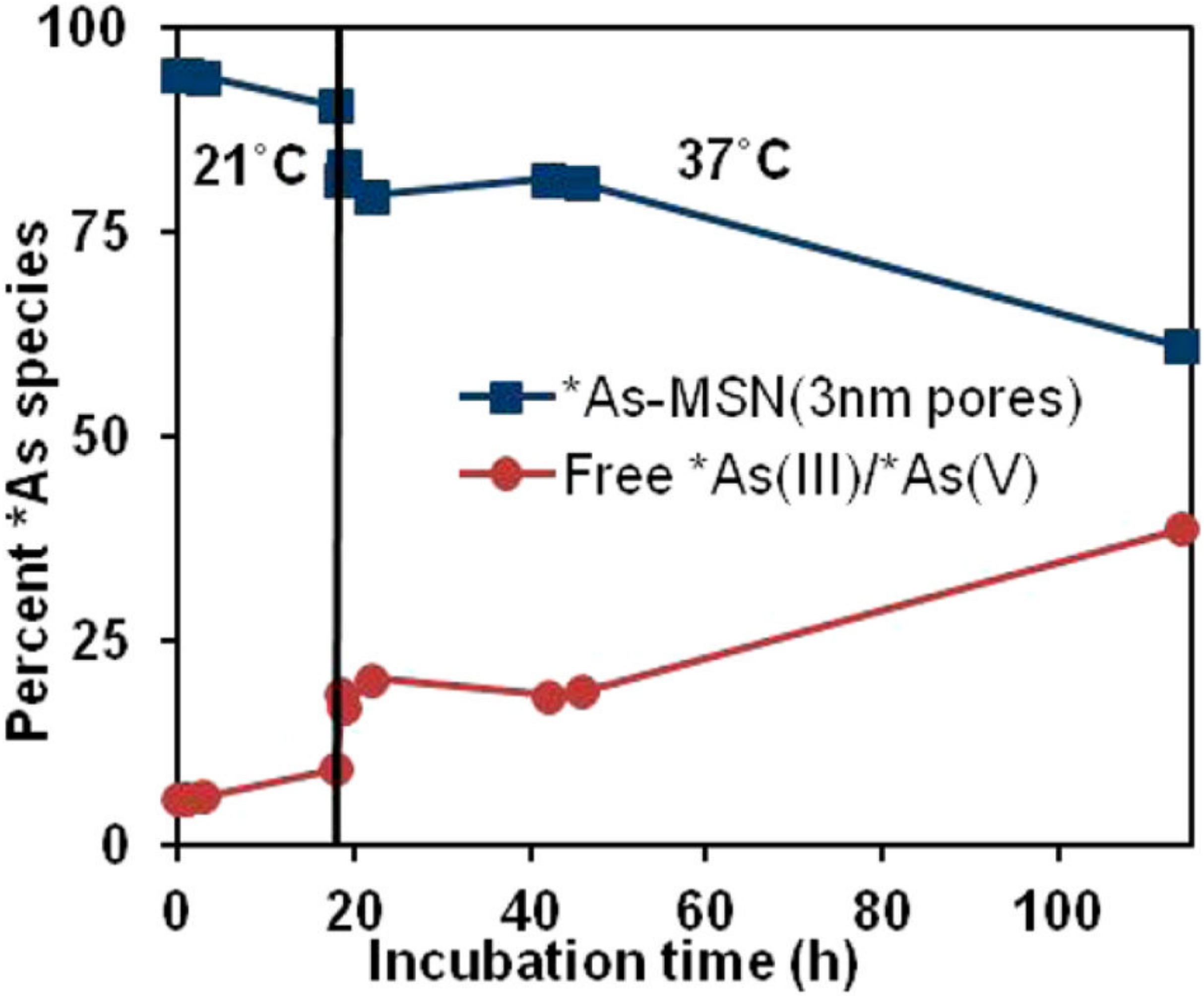

Figure 5.

Stability of centrifugation/decantation-isolated *As-MSN (3 nm pores) reformulated in whole mouse serum and incubated at 21 and 37 °C. While uncertainties were not quantified in these radio-TLC studies, the methods resulted in high uncertainty estimated to be ~15% in solutions containing nearly 0% *As(III)/*As(V) and nearly 100% *As-MSN (3 nm pores).

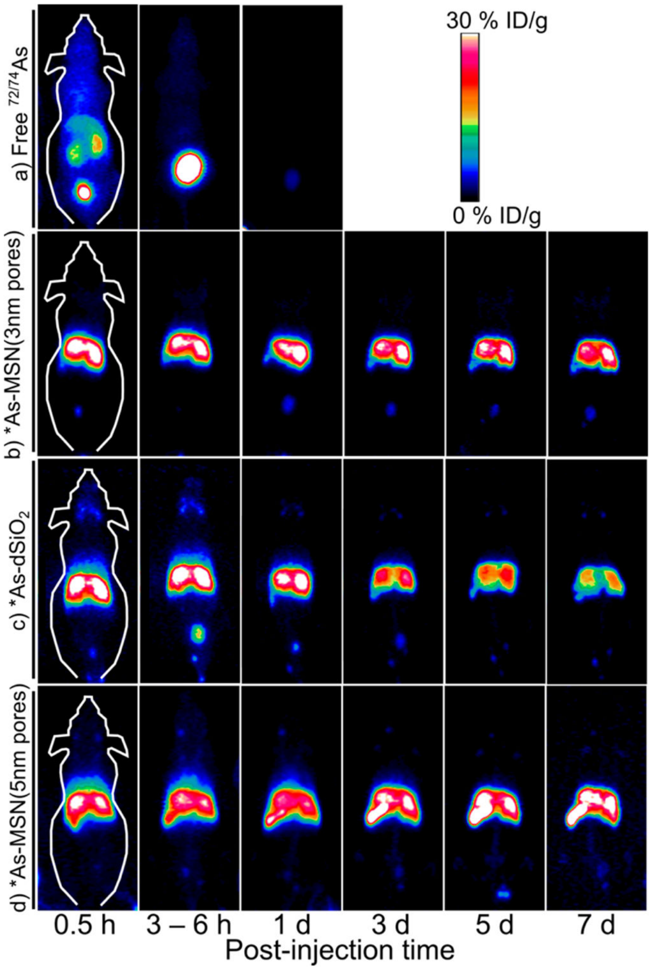

Figure 6.

Serial MIP PET images of healthy BALB/c mice following iv administration of (a) free *As, (b) *As-MSN (3 nm pores), (c) *As-dSiO$_2$, and (d) *As-MSN (5 nm pores).

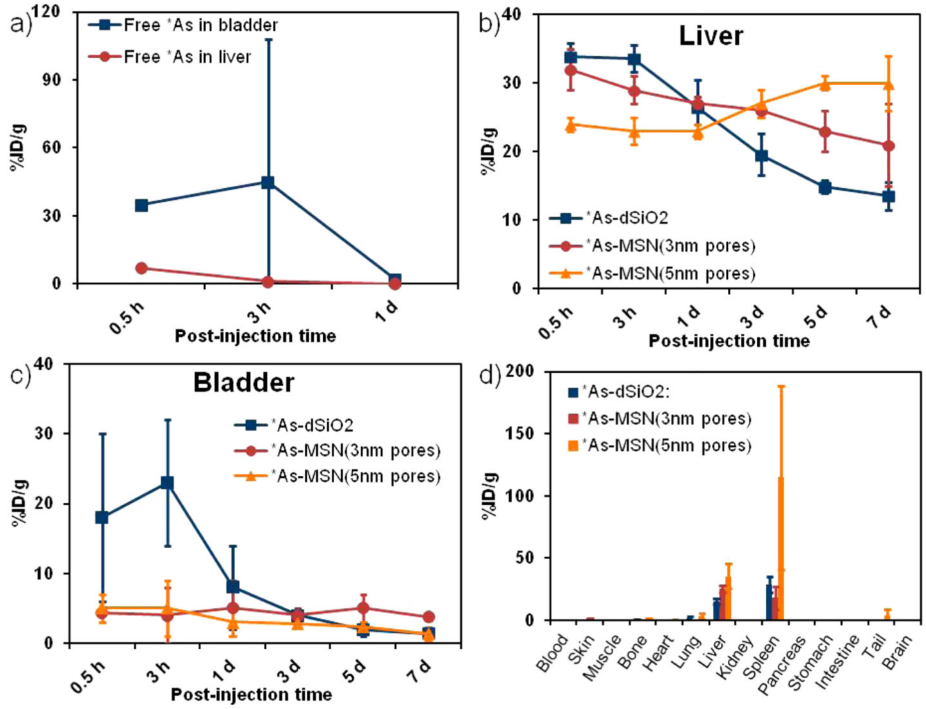

Figure 7.

Average PET-quantified percent injected dose per gram (%ID/g) in healthy mice (*n* = 3) of iv administered free *As (a), *As-MSN(3 nm pores), *As-dSiO$_2$, and *As-MSN(5 nm pores) in the liver and bladder (b, c) as a function of time postinjection. (d) *Ex vivo* biodistribution of *As-dSiO$_2$, *As-MSN(3 nm pores), and *As-MSN(5 nm pores) 7 days postinjection in healthy mice (*n* = 3).

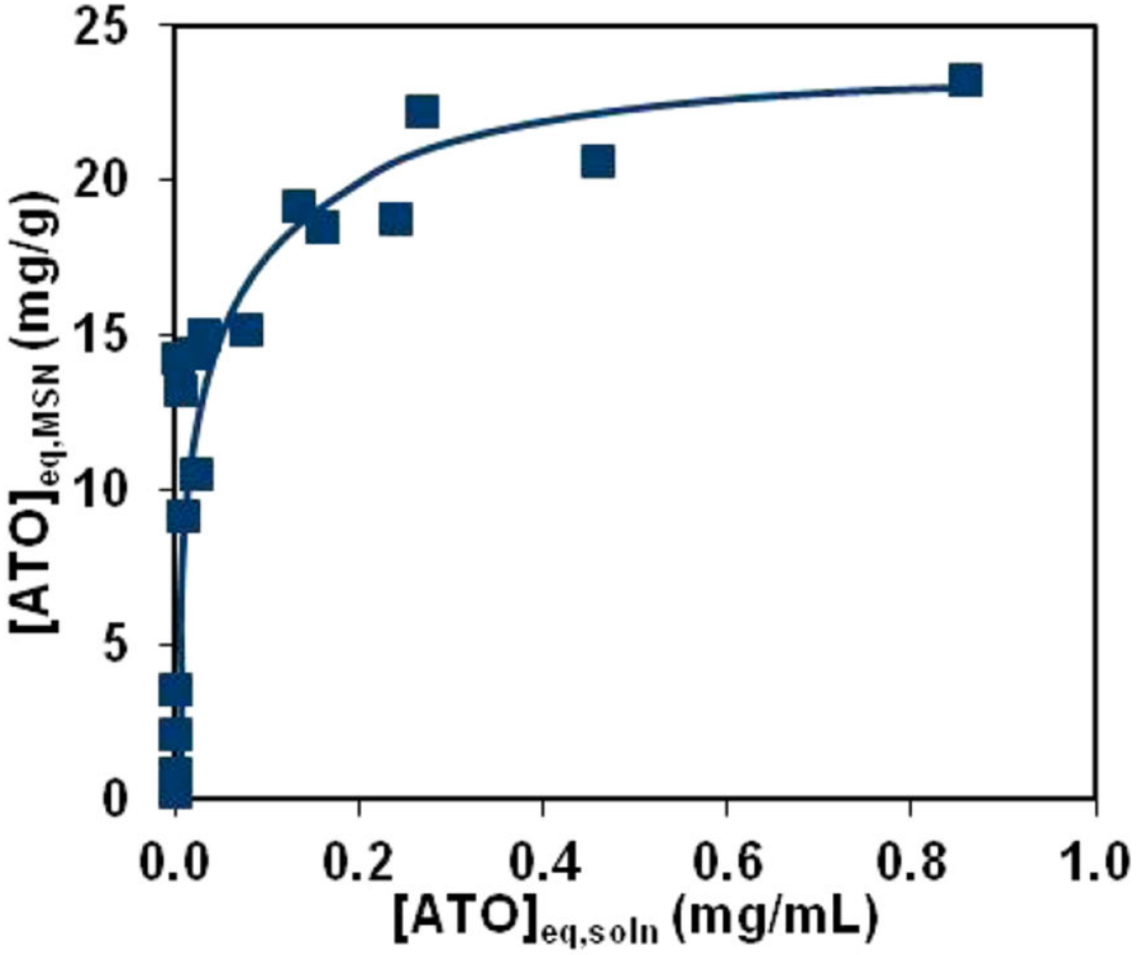

Figure 8.

Results of ATO loading capacity experiments plotted as equilibrium ATO mass bound to MSN(5 nm pores) in mg ATO per g of MSN as a function of ATO mass left unbound in solution in mg ATO per mL of solution. Uncertainties in $[ATO]_{eq,MSN}$ quantified from triplicate MP-AES measurements were measured to be less than or equal to ~1 mg/g. Line drawn to guide the eye.

Table 1

Physical Properties of Thiol-Modified Silica Nanoparticles Used in This Work

	diameter (nm)	pore diameter (nm)	zeta potential (pH 5–6 H_2O, mV)	surface area per particle (nm^2)	thiols per particle
$dSiO_2$	90 ± 10	no mesopores	−36 ± 1	3.2×10^4	2.3×10^6
MSN (3 nm pores)	65 ± 5	~3	−44 ± 2	3.5×10^4	5.6×10^6
MSN (5 nm pores)	150 ± 5	~5	−44 ± 1	5.6×10^5	2.2×10^8